Mixing Strategies for Zinc Oxide Nanoparticle Synthesis via a Polyol Process

Mongia Hosni, Samir Farhat, Mounir Ben Amar, Andrei Kanaev, and Noureddine Jouini
Laboratoire des Sciences des Procédés et des Matériaux, LSPM-CNRS,
Université Paris 13, 99 av. J. B. Clément 93430 Villetaneuse, France

Ivaylo Hinkov
Dept. of Chemical Engineering, University of Chemical Technology and Metallurgy - 8 St. KlimentOhridski Blvd,
1756 Sofia, Bulgaria

DOI 10.1002/aic.14737

We report on the effect of mixing on the morphology of ultrafine zinc oxide nanoparticles synthesized via a polyol process using zinc acetate and water in a diethylene glycol medium. Three mixing strategies were considered: stirred batch, T-mixer, and impinging free jets. The particle granulometry was accessed using the transmission electron microscopy and x-ray diffraction methods. The nanoparticle size and polydispersity decreased with an increase in the local dissipated energy. In particular, the polyol process conducted in the same chemical environment at 353 K did not lead to the observation of nanoparticles in the stirred batch reactor but resulted in unconventionally small 6-nm particles in the T-mixer and impinging jet configurations. This result is apparently related to the micromixing eddy geometry described by the Kolmogorov length. The hydrodynamic flow patterns and energy dissipation were obtained from computational fluid dynamics simulations, which are essential in the design, optimization, and scale-up of the polyol process. © 2015 American Institute of Chemical Engineers *AIChE J*, 61: 1708–1721, 2015
Keywords: mixing, zinc oxide, nanoparticles, growth, computational fluid dynamics modeling

Introduction

Due to the short induction periods and high nucleation rates during precipitation, turbulent mixing can become a controlling factor for rapid chemical precipitation in liquid media at scales ranging from large lengths similar to the reactor geometry down to the molecular or micro scale. Indeed, mixing changes the supersaturation distribution throughout the reactor, thereby affecting the precipitation rate and particle size distribution. Since the pioneering work of Kolmogorov,[1] this topic has been intensively studied under the classical precipitation context[2–4] and subsequently extended to nanoparticle synthesis.[5–9]

The most common configuration of the mixing reactor used in precipitation is the stirred reactor in which different types of impellers produce the different flow fields.[10–12] Decreasing the dimensions of the reactors to submillimeter size, that is, the T-mixer[5–9,13] or the two-impinging-jets (TIJ) mixer,[14] offers advantages with respect to heat and mass transfer due to rapid mixing times. Recently, experimental and theoretical methods for estimation of macro- and micro-scale mixing were reviewed within the context of nanomaterials in the book by Bockhorn et al.,[15] and experimental evidence collected by particle image velocimetry and laser-induced fluorescence support the hypotheses that the precipitation of nanoparticles requires high mixing intensity and that the mean particle sizes and the width of the particle size distribution both decrease as the mixing intensity increases.

To further assess the role of mixing, modeling of the particle size distribution of the precipitation process was performed via coupling of computational fluid dynamics (CFD) with the micromixing model and with the solid model of the direct numerical simulation–population balance equation (DNS–PBE) approach. Population balance equations (PBEs) have been successfully implemented to predict particle and crystal formation dynamics.[16–21] Because mixing is an important aspect of precipitation modeling, several works[6,22–26] have attempted to couple the PBEs with CFD to investigate the impact of various steps on the nanoparticle size distribution. These steps include nucleation, growth, turbulent mixing, agglomeration, breakage, and so forth, and the coupling among them in various types of reactors, that is, stirred batch reactors with simple or multiple feeds,[27,28] Couette-type precipitators,[29] confined impinging jets (CIJ),[7,30–32] and multi-inlet vortex (MIV)[33] reactors. The Navier–Stokes fluid dynamics equations are generally solved using the Reynolds averaging approach (RANS) formulation, and mixing models were added to account for mixing at scales less than the grid resolution.[6,22] The coupling of RANS-based CFD with the population balance approach was considered[34] for the gas-phase synthesis of nanoparticles.

To simulate precipitation in stirred tank reactors, instead of CFD, certain models used a compartmental mixing model that required less CPU time.[35] The CPU time requirements

---

Correspondence concerning this article should be addressed to S. Farhat at samir.farhat@lspm.cnrs.fr

for these approaches are moderate, but the capacity for predicting the distribution width is poor due primarily to differences in mixing histories. To include temporal and spatial fluctuations in the flow through the mixer, direct numerical simulation (DNS) was coupled with the population balance model (PBM) using a Lagrangian approach.[7] More recently, reactive kinetics coupled with the PBM and CFD was implemented to simulate silver nanoparticle formation in a microtubular reactor.[36] Numerical methods to solve the PBE coupled to a computational fluid dynamics (PB-CFD) simulation have been recently reviewed in the light of robustness, accuracy, and CPU time.[37] Phenomenologically, slow diffusional mixing of reagents will lead to an incompletely mixed fluid that causes heterogeneity in particle size. In contrast, turbulence characterized by low momentum diffusion, high momentum convection, and rapid variation of pressure and velocity in space and time can improve mixing efficiency. This process brings liquid reagents into contact easily, thus affecting the reaction kinetics and particle formation as well as the resulting product properties.

This process is of primary importance for particles with sizes under the limit of 100 nm, which are referred to as ultrafine nanoparticles. Indeed, certain conducting and semiconducting materials exhibit size-related optical, electronic, and magnetic properties that differentiate them from their bulk counterparts. This interesting class of nanomaterials is used as advanced functional materials with promising high technology applications in photovoltaics, sensory probes, therapeutic agents, drug delivery, electronic conductors, and catalysis. Nevertheless, key issues related to ultrafine nanoparticles include methods for growing them in a controlled manner and strategies for scale-up of their fabrication. Among the different synthesis techniques available, bottom-up assembly is powerful for creating identical engineered structures with atomic precision and few defects. This approach uses homogeneous nucleation from the liquid or vapor phase or heterogeneous nucleation on substrates. This process includes different classes of processes, that is, hydrothermal, sol-gel, microemulsion, and polyol synthesis, often with thermal, microwave, or ultrasonic activation.

Due to its simplicity and versatility, the polyol-mediated route is an interesting bottom-up process proposed for the synthesis of different metal and oxide nanomaterials and was recently reviewed by Fiévet and Brayner.[38] The polyol process was first developed to produce finely divided metallic powders and was patented in 1985.[39] Due to their hydrogen bonds and relatively high dielectric constant, polyols act as solvents that can dissolve the majority of inorganic precursors as metallic salts. In addition, due to their chelating properties, polyols can also play the role of coordinating solvents, complexants, and surfactants that adsorb on the elementary particle surface during growth, thus preventing agglomeration. These materials also allow two competitive chemical reactions to occur: reduction and forced hydrolysis. If water is absent in the medium, reduction is favored, and metal can be obtained starting from dissolved metal salts. The presence of water favors forced hydrolysis, which leads to the formation of hydroxides and oxides.[40] At the laboratory scale, this method already provides rigorous control of the size and shape of such nanomaterials as zinc oxide nanoparticles via adjustment of the reaction stoichiometry, that is, hydrolysis ratio and basicity.[41] Nevertheless, other parameters, that is, the efficiency of mixing reagents, could affect the particle size distribution, especially if working with highly viscous media, that is, polyols and fast and irreversible precipitation reactions of the type

$$A^{n+} + B^{n-} \rightarrow C\downarrow$$

where A and B are the reagents and C is the reaction product that accounts for the nanoparticles obtained by subsequent nucleation and growth. Indeed, contrary to the mixing of gases, which is entirely ensured by molecular diffusion, even at low Reynolds numbers (*Re*), rapid mixing remains necessary for the liquid phase due to the small diffusion constants of the liquids. After mixing of reagents, precipitation is the result of several mechanisms, that is, nucleation, growth, and secondary processes such as agglomeration and ripening. Nucleation is the formation of a solid phase from the liquid; this process occurs when a critical number of molecules join together to form a thermodynamically stable aggregate that grows into larger particles via precursor addition. Nucleation and growth are competing phenomena because both steps consume precursor molecules, and therefore, particle size is the result of this competition. Notably small particles are produced by high nucleation rates, whereas large particles are produced by low nucleation rates. Hence, because mixing and reaction are connected, the manner in which reagents are mixed can significantly influence the final particle size distribution. Although these characteristics are crucial for the above-discussed applications, improving the design and performance of mixing systems for nanoparticle synthesis is crucial. This topic has matured over the years, mostly through trial-and-error approaches, and the requirement exists for a fundamental basis upon which to estimate a mixer's performance, especially in the nanoparticle context in which time and length scales are notably small. Understanding the hydrodynamics in this context will provide guidelines for the design of particles with well-defined characteristics such as a uniform shape, narrow size distribution, high surface area, and low degree of agglomeration.

The effect of mixing on nanoparticle size was demonstrated for mixers ranging from stirred reactors to T-mixers.[15] Two important parameters appear to affect particle size distribution: the flow rates of reagents or *Re* and the energy dissipation (ε). Increasing both of these parameters permits a reduction in particle size and decreases the distribution width. For example, increasing specific energy dissipation (ε) from 1 W/kg to approximately 10^5 W/kg decreases the cadmium sulfide (CdS) nanoparticle size from 10 to 4 nm.[15] The same behavior was observed by Azouani et al.[42] for titanium oxide (TiO_2) nanoparticle synthesis via turbulent T-mixing. Control of the injection time of the reagents permits the separation of nucleation and growth steps and allows the synthesis of TiO_2 nanoparticles as small as 4 nm in diameter, as measured by a light-scattering technique. In the same direction, increasing the reagent flow rates by one order of magnitude permits a narrower particle size distribution and reduces the average diameter of molybdenum sulfide (MoS_2) nanoparticles by a factor of nearly 2, as demonstrated by Santillo et al.[43] Additionally, Winkelmann et al.[44] investigated the influence of mixing on the precipitation of zinc oxide nanoparticles. In increasing the mixing quality by decreasing the nozzle diameter, the mean particle size was reduced from 120 to 35 nm. No further reduction of the particle size was possible by changing the nozzle geometry size. More recently, Bensaid et al.[45]

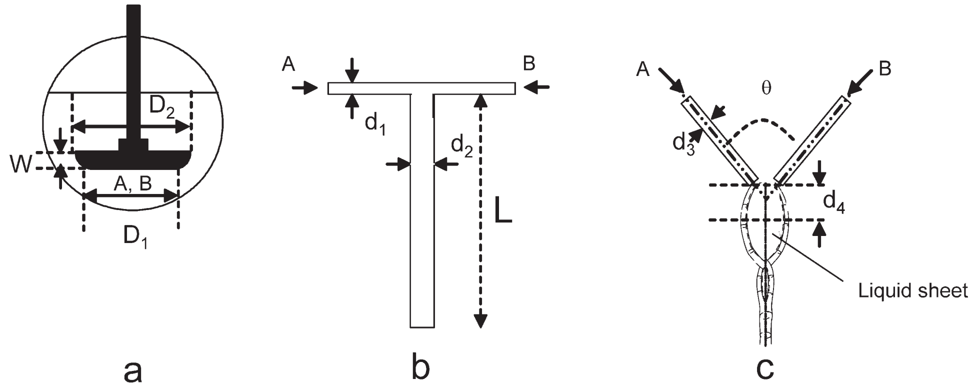

Figure 1. Mixing geometries.

(a) Stirred reactor with straight paddle diameters $D_1 = 5$ cm, $D_2 = 7$ cm and width $W = 1$ cm; (b) T-mixer input diameter $d_1 = 1$ mm, output diameter $d_2 = 2$ mm, length $L = 20$ cm; and (c) Impinging free jet mixer: needle internal diameter $d_3 = 584$ μm or $d_3 = 394$ μm and $d_4 = 3$ mm and $\theta = 45°$.

controlled the synthesis of MoS_2 nanoparticles by MIV mixing. Increasing the *Re* in the mixing chamber by one order of magnitude decreases the nanoparticle size from 135 to 60 nm. CFD simulations were performed to further assess the mixing efficiency.

Additionally, impinging jets are one of the generic configurations used for atomization and mixing and were originally proposed in liquid propellant engines.[46] A rich variety of flow structures have been observed, from a single oscillating jet obtained at low flow rates to the violent disintegration of flapping sheets obtained at higher flow rates, depending on the Weber and *Re* of the jets.[47]

In this work, the effects of mixing on the zinc oxide nanoparticle synthesis via a polyol medium are studied for different geometric configurations. Because the flow of a reacting fluid is a highly complex process, idealized mixing strategies were tested, including batch-stirred reactors, impinging jets, and T-mixers. The relationship between the hydrodynamic features during the synthesis and the final size and shape of nanoparticles was examined using structural and morphological analysis and CFD calculations.

Experimental

Chemicals and materials

Zinc acetate dihydrate [$(Zn(OAc)_2{\cdot}2H_2O)$] and diethylene glycol (DEG) [$O(CH_2CH_2OH)_2$] were purchased from Sigma-Aldrich. Distilled water was added to adjust the hydrolysis ratio, and ethanol and acetone were used for the washing and cleaning of nanoparticles. All chemicals were of analytical grade and were used without further purification. To control the reaction stoichiometry, we defined the metal concentration in the polyol solution as $z = [Zn^{2+}]$ mol L^{-1} and the hydrolysis ratio as $h = \frac{n_{H_2O}}{n_{Zn^{2+}}}$, where n_{H_2O} and $n_{Zn^{2+}}$ account for the number of moles of water (including those of zinc acetate dihydrate) and zinc precursor, respectively.

As we demonstrated in our previous work,[48] the size and morphology of zinc oxide nanoparticles obtained by the polyol process could be controlled by adjusting the zinc molar concentration *z*, the hydrolysis ratio *h* and an additional parameter, defined as the alkaline ratio, $b = \frac{n_{NaOH}}{n_{Zn^{2+}}}$ with n_{NaOH} the number of sodium hydroxide moles deliberately added to control the morphology. Indeed, the relative growth rates of the ZnO crystal facets could be modified by adjusting the three parameters *h*, *b*, and *z*, thereby controlling the final shape and size of the crystal. Since we focus this study on the mixing effects, the stoechiometry of the hydolysis reaction was simplified to consider only one pair of reactants, that is, zinc cation Zn^{2+} controlled by the parameter *z* and water controlled by *h*.[48]

Mixing configurations

The three mixing geometries shown in Figure 1 were used for zinc oxide nanoparticle synthesis under a DEG polyol medium. To dissociate mixing and stoichiometric effects, all synthesis was conducted under the same stoichiometric parameters, that is, $z = 0.2$ mol L^{-1} and $h = 5$.

For the stirred batch configuration, a spherical three-neck glass reactor equipped with a mechanical agitator and Pt100 thermocouple was used (Figure 1a). Zinc acetate dihydrate and an appropriate amount of distilled water were dissolved in 200 mL of DEG and heated to 353 or 403 K for 1 h under continuous stirring. For mixing of the reagents, a straight impeller that generates axial-like features was powered by a Heidolph RZR-2021 motor, and the speed was maintained at approximately 220 rpm during the entire experiment. The impeller blade width and diameters were $W = 1$ cm, $D_1 = 5$ cm, and $D_2 = 7$ cm, respectively.

For the T-mixer synthesis, we used the reactor described in detail in Ref. [21, which was composed of two flow-input tubes with an internal diameter $d_1 = 1.0$ mm. After exocentric fluid injection, the flow exits the system from an output tube that is 20 cm in length. To conserve the *Re* between the input and the output, the external diameter was chosen as $d_2 = 2.0$ mm. Two solutions, respectively, containing zinc acetate (A) with DEG and distilled water (B) with DEG were injected into the countercurrent, as shown in Figure 1b. The flow rate in the T-mixer was maintained by submitting the solutions in the buffer reservoirs to a pneumatic pressure of nitrogen gas at $P = 6 \times 10^5$ Pa. Because the T-mixer exit is at atmospheric pressure, the pressure drop through the system ($\Delta P = P - 1.01 \times 10^5$ Pa) ensures a continuous flow. During the mixing, the buffer reagent solutions as well as the input and output tubes were maintained at 353 K by circulating water through the external jacket and thermo-controlled reservoir.

For the free impinging jet configuration, the diameter of the injection tube was reduced to approximately 400 μm, and the mixing zone did not contact any other surfaces, as

Table 1. Experimental Conditions for the Zinc Oxide Synthesis in Different Mixing Configurations with $z = 0.2$ mol L^{-1} and $h = 5$

Experiment n°	Mixing configuration	Conditions
Z0	Stirred reactor	$N = 220$ rpm $T = 353$ K$\mu = 4.718$ c$P\rho = 1.074$ g cm^{-3} Re[a] $= 1801$ Sc[b] $= 4393$
Z1	Stirred reactor	$N = 220$ rpm $T = 403$ K$\mu = 1.325$ c$P\rho = 1.034$ g cm^{-3} $Re = 6187$ $Sc = 789$
Z2	Impinging jet	$d_3 = 394$ µm $t_{\text{inj}} = 16$ s $T = 353$ K$\mu = 4.718$ c$P\rho = 1.074$ g cm^{-3} $v = 5.12$ m s^{-1} $Re = 459$ $Sc = 4393$
Z3	Impinging jet	$d_3 = 584$ µm $t_{\text{inj}} = 7$ s $T = 353$ K$\mu = 4.718$ c$P\rho = 1.074$ g cm^{-3} $v = 5.33$ m s^{-1} $Re = 709$ $Sc = 4393$
Z4	T-mixer	$\Delta P = 5 \times 10^5$ Pa $T = 353$ K$\mu = 4.718$ c$P\rho = 1.074$ g cm^{-3} $v = 8.04$ m s^{-1} $Re = 1830$ $Sc = 4393$

[a] The turbulent regime is generally considered fully developed at Reynolds numbers $Re > 1000$ in small stirred reactors[49] and $Re > 500$ in a T-mixers.[5,50,51]
[b] Schmidt number Sc is calculated from the kinematic viscosity v and the diffusion coefficient of species D_{AB} estimated from Wilke and Chang equation for diffusion in liquids.[52]

shown in Figure 1c. This process was performed using two glass syringes (Furtuna Optima) equipped with a stainless steel syringe gauge of 20 or 22. For the 20-gauge syringe needle, the internal diameter was $d_3 = 584$ µm, and for the 22-gauge syringe, the internal diameter was as small as $d_3 = 394$ µm. These needles form an angle of $\theta = 45°$, and the mixing point was maintained at a distance $d_4 = 3$ mm from the orifice of the needles. The reactant was injected at 353 K, and the flow rate was calculated from the measured injected volume and injection time. Because the injections were performed in ambient air, the fluid exiting the impinging jet was received in a collection vessel where it was maintained at 353 K without any further mixing.

The experiments discussed above are summarized in Table 1, in which the Re was calculated from $Re = \frac{\rho N D^2}{\mu}$ for the agitated vessel and $Re = \frac{\rho v d}{\mu}$ for the T-mixer and free impinging jet. In these equations, N is the agitation speed, D is the paddle average diameter, and d is the internal diameter of the injection tube. As a first approach, the Re numbers were calculated using the temperature-dependent viscosity μ and mass density ρ of the polyol, that is, DEG, and the effects of nanoparticles on μ and ρ were neglected.

Zinc oxide synthesis and characterization

The three mixing strategies were applied under the previously discussed experimental conditions. For the batch reactor, the transparent reagents were mixed and heated simultaneously, and nucleation and growth occurred when the solution color shifted to white. For the T-mixer and free jet configurations, the reagents were injected separately at the specified temperature. All experiments led to a white colloidal suspension, except for experiment Z0 performed in the batch-stirred configuration at 353 K, in which no visible precipitate was observed. In contrast to experiments Z2–4, it may seem contradictory from thermodynamics point of view, that the experiment Z0 conducted at the same temperature does not produce stable nanoparticles. Regarding the solution transparency, two assumptions can be made: (i) zinc oxide was not produced in the stirred rector since intense micromixing of reactants is needed to create supersaturation before the nucleation starts as in the T-mixer and impinging jet configurations; or (ii) particles created in the stirred reactor have very small sizes to be experimentally observed. To verify these assumptions, the Z0 solution was exposed to a laser beam, and no scattering from particles was observed. Additionally, dynamic light scattering measurements at the limit of detection of approximately1 nm did not show any signal, suggesting that supersaturation was not reached as assumed in assumption (i). Standard UV–Visible absorption spectra are not applicable for subnanometer diameters since there is a dependence of the optical properties of nanoparticles on their size.[53] Theoretical explanations of this behavior lies with the dependence of surface plasmon resonance peak with the size of the nanoparticule as discussed by Haiss et al.[53] Nevertheless, the possibility of quantum dot formation with a size smaller than approximately 1 nm exists, supporting assumption (ii). Indeed, Caetano et al.[54] observed ZnO quantum dots via in situ time-resolved UV–Vis absorption spectra combined with small-angle x-ray scattering and x-ray absorption fine structure. The suspensions obtained in experiments Z1–Z4 were centrifuged, filtered, and washed several times, and the white solid powders were dried and subsequently characterized using a JEOL 2011 transmission electron microscope (TEM) operating at 200 kV. During washing the nanoparticles with acetone and ethanol agglomeration is obviously inevitable since the chelating polyol is removed. Then, the acetone and ethanol solvent evaporation dynamics and the wetting behavior of the solvent affect this agglomeration kinetics. Nevertheless, further growth of the nanoparticle during washing and drying processes is unlikely without sufficient thermal activation. The measurements of individual nanoparticle size were performed by assuming spherical particles, using image analysis software to determine the cross-sectional area of the particles, and converting the area to an equivalent spherical diameter. A statistical analysis was performed on at least 100 nanoparticles from several TEM images. To further confirm the zinc oxide phase and morphology, x-ray diffraction data were collected in the 2θ angle range from 30° to 80°. The X-ray diffraction (XRD) analysis was performed using 2INELTM diffractometers with Cu-Kα1 radiation. The nanocrystallite sizes were calculated using Scherrer's Eq. 1

$$D_{hkl} = \frac{k\lambda}{B\cos(\theta)} \tag{1}$$

where λ is the x-ray radiation wavelength ($\lambda = 1.5406$ Å), θ is the Bragg's angle at which the peak is observed (measured in radians), and B is the full width of the diffraction line at half of the maximum intensity.[55,56]

Results and Discussion

The effect of mixing on particle growth and agglomeration is quite evident from the TEM micrographs. As shown in Figure 2, different sizes and degrees of agglomeration were observed for experiments Z1–Z4. Indeed, the TEM micrographs display secondary polycrystalline ZnO nanoparticles composed of several uniform primary ZnO subcrystals of the same crystal orientation. It may be possible that van der Waals interactions between the surfaces of the nanocrystallites are the driving force for self-assembly. Due to the

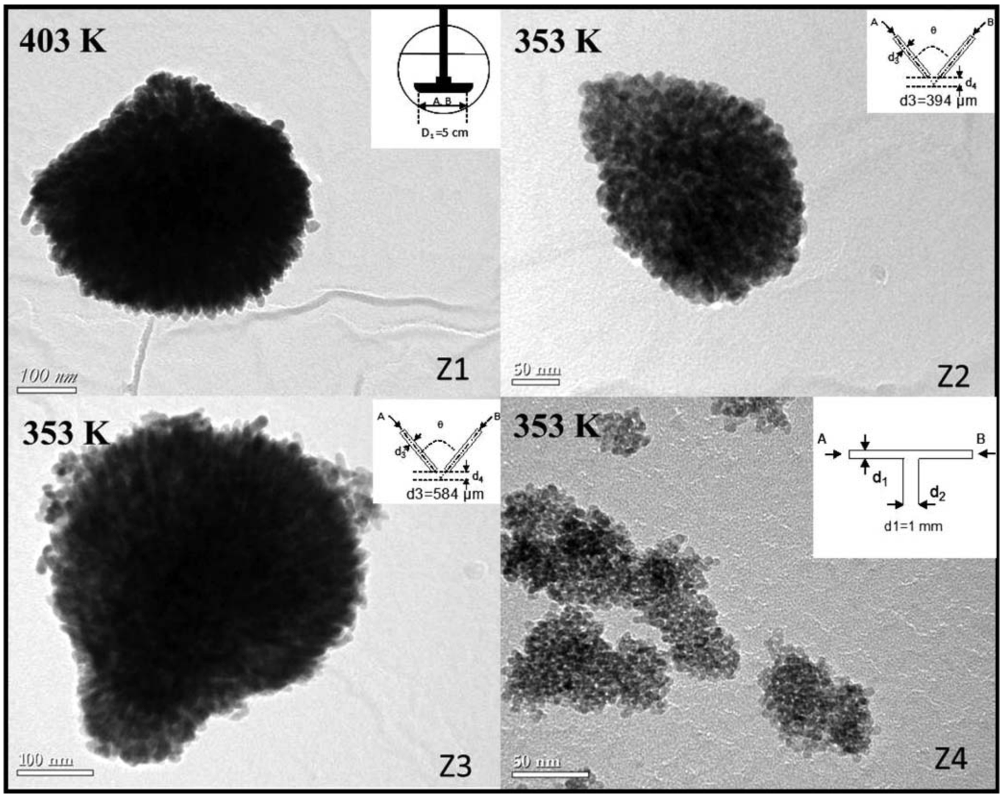

Figure 2. TEM micrographs of ZnO nanoparticles obtained in different mixing systems referenced in Table 1.

(Z1) stirred batch reactor at 403 K. (Z2) impinging jets with 394 μm syringe diameter. (Z3) impinging jet at 353 K with 584 μm syringe diameter. (Z4) T-mixer at 353 K.

chelating effects of DEG, primary particles grow separately, and due to their high surface reactivity, they subsequently assemble to form secondary ZnO nanoparticles. Agglomeration is obviously inevitable during washing of the nanoparticles with acetone and ethanol solvents because the chelating polyol is removed from the nanoparticles. Additionally, the acetone and ethanol solvent evaporation dynamics and the wetting behavior of the solvent affect the agglomeration kinetics. Agglomeration is clearly shown in the TEM pictures of Figure 2. Nevertheless, further growth of the nanoparticles during the washing and drying processes is unlikely without sufficient thermal activation. The particle size distribution was determined by statistical analysis performed on the individual particles from the TEM pictures, and the results are plotted in Figure 3. For batch reactor synthesis experiment number Z1, particles with an average diameter of approximately19 nm agglomerated in larger clusters that were synthesized. For the free impinging jet samples, the individual particle average sizes are approximately13 nm for Z2 and approximately10 nm for Z3. When the T-mixer was used, the average individual particle size obtained in the Z4 sample was drastically lowered to approximately 6 nm, and these particles were less agglomerated, as shown in Figure 2.

From the particle size distributions shown in Figure 3, we can conclude that the stirred reactor (Z1) presents the largest particle size and the largest particle size distribution, whereas the impinging free jets produced intermediate sizes and distributions. In contrast, the T-mixer allows for the smallest particle diameters and the narrowest diameter distribution.

X-ray diffraction data were collected to further confirm that the nanoparticles consist of zinc oxide. The XRD patterns of samples Z1–Z4 are shown in Figure 4 and are in agreement with the standard x-ray diffraction peaks, which confirm that the synthesized materials are well crystallized.

From Figure 4, we can conclude that the peaks obtained from the T-mixer are broader than those obtained from the impinging jet and stirred reactor, thus confirming the smaller particle size observed in the TEM micrographs. In addition, the XRD crystallite sizes calculated from Scherrer's equation

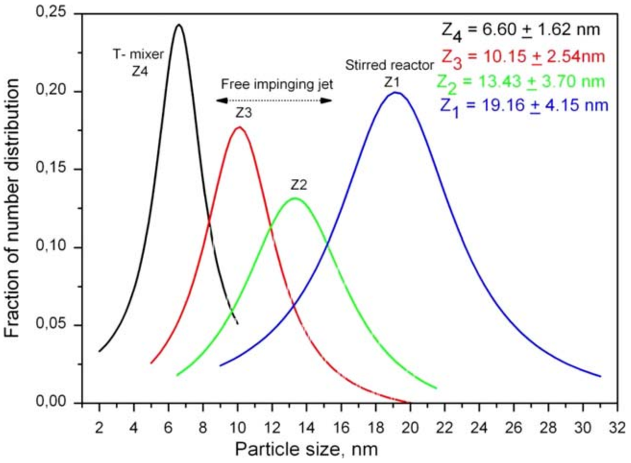

Figure 3. Diameter distributions of ZnO nanoparticles obtained from TEM micrographs.

(Z1) stirred batch reactor at 403 K; (Z2) impinging jets with 394 μm syringe diameter; (Z3) impinging jet at 353 K with 584 μm syringe diameter; and (Z4) T-mixer at 353 K. [Color figure can be viewed in the online issue, which is available at wileyonlinelibrary.com.]

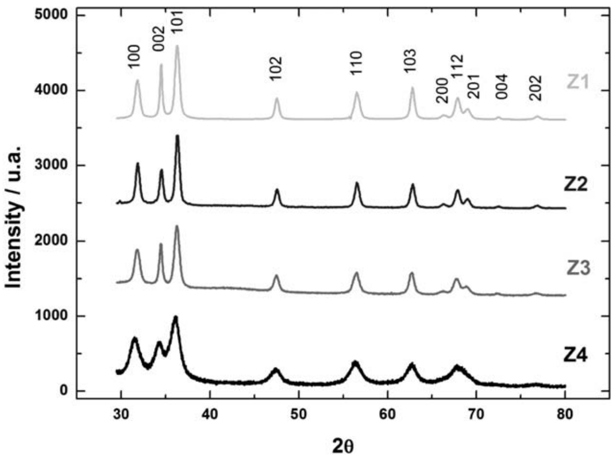

Figure 4. XRD patterns of the powder obtained under different mixing configurations.

Positions of the zinc oxide peaks are indexed. (Z1) stirred batch reactor at 403 K. (Z2) impinging jets with 394 μm syringe diameter. (Z3) impinging jet at 353 K with 584 μm syringe diameter. (Z4) T-mixer at 353 K.

and reported in Table 2 are similar to those obtained from TEM analysis, indicating that the nanoparticles are monocrystalline. However, the lattice constants a and c confirm the hexagonal Wurtzit zinc oxide structure. The data of Table 2 are consistent with the literature reviewed data. The lattice constants of zinc oxide Wurtzit crystal mostly range from 3.247 to 3.286 Å for the a-parameter and from 5.204 to 5.241 Å for the *c*-parameter.[57]

For the stirred tank, species will have sufficient time for diffusion at the molecular scale. Nevertheless, the high viscosity, and therefore, the high Schmidt number in the polyol slow these mixing effects, and nucleation occurs only when the temperature reaches the steady-state value of 403 K. In contrast, due to the high energy dissipation rate (approximately 9×10^4 W kg^{-1}) in the T-mixer, the reaction occurs at a temperature of 353 K, which is much lower than in the stirred system. Hence, we can conclude that chemical reaction can be enhanced by improved mixing.

To qualitatively explain these results, we must consider the chemical reactions between reagents and their turbulence behavior under each mixing situation. For the kinetics of zinc oxide growth, the commonly accepted mechanism[58,59] is the forced hydrolysis of zinc acetate in DEG, which leads to different zinc complexes in reaction (r_1). These complexes dehydrate and remove acetic acid to form pure ZnO in reaction (r_2). Both steps (r_1) and (r_2) are thermally activated.

$$\mathrm{Zn(CH_3COO)_2} + x\mathrm{H_2O} \xrightarrow{\Delta,\mathrm{DEG}} \mathrm{Zn(OH^-)}_x\mathrm{(CH_3COO^-)}_{2-x} + x\mathrm{CH_3COOH} \qquad \text{(r1)}$$

$$\mathrm{Zn(OH^-)}_x\mathrm{(CH_3COO^-)}_{2-x} \xrightarrow{\Delta,\mathrm{DEG}} \mathrm{ZnO} + (x-1)\mathrm{H_2O} + (2-x)\mathrm{CH_3COOH} \qquad \text{(r2)}$$

To the best knowledge of the authors, no quantitative kinetics data are available for these reactions in the published literature. Nevertheless, in a conventional laboratory reactor, it was reported[59] that these two reactions proceed simultaneously and are thermally activated because they occur at temperatures above 383 K. Hence, it is quite evident that experiment Z0 conducted at 353 K did not lead to any precipitation because the thermal activation barrier was not reached. Bilecka et al.[60] studied the kinetic and thermodynamic aspects of the microwave-assisted synthesis of ZnO nanoparticles from zinc acetate and benzyl alcohol in a nonaqueous medium.

For the stirred reactor, increasing the temperature from 353 to 403 K improves both the rate of reaction and the mixing because the *Re* is significantly increased from 1801 to 6187, thereby intensifying the macroscale and consequently the microscale mixing; this is an important characteristic of the polyol process in which viscosity is highly dependent on temperature as fitted from experimental data.[61]

For the impinging free jet and T-mixer, the smaller characteristic mixing length scale increases the local turbulence intensity, thus rendering the mixing process faster than nucleation. Hence, the nucleation rate is improved, the average size of particles is decreased, and a much more uniform particle size distribution is obtained, as shown in Figure 3.

Mixing time

To quantitatively explain these results, one must consider the process of turbulent mixing under each previously discussed mixing situation. Nevertheless, this situation is highly complex, largely because turbulent mixing involves a wide range of time and length scales. Indeed, mixing is initiated at the macroscale level and proceeds in a cascade-like manner down to the microscale level.[62] However, chemical reactions can only take place when the reacting species come into contact at the microscale level defined by elementary eddies in the fluid and characterized by the Kolmogorov length scale L_K given by Eq. 2

$$L_\mathrm{K} = \left(\frac{\upsilon^3}{\varepsilon}\right)^{\frac{1}{4}} \qquad (2)$$

where v is the kinematic viscosity of the fluid and ε is the specific dissipated turbulent power.

In the case of stirred tanks, as reported in Ref. [63, ε can be estimated from the power P used to drive the impeller, the fluid volume V, and the mass density ρ using Eq. 3

$$\varepsilon = \frac{P}{\rho V} \qquad (3)$$

For a given stirring speed N, the average power consumption can be estimated from the impeller diameter D and

Table 2. Zinc Oxide Nanoparticle Sizes as Obtained from TEM and XRD Analysis

Sample	Size from TEM (nm)	Size from XRD (nm)	Lattice constants *a* and *c* (Å)
Z1	19.16 ± 4.15	$D_{(100)} = 14.58$ $D_{(002)} = 14.46$ $D_{(101)} = 18.35$	$a = 3.260$ $c = 5.223$
Z2	13.43 ± 3.70	$D_{(100)} = 11.95$ $D_{(002)} = 14.47$ $D_{(101)} = 9.93$	$a = 3.263$ $c = 5.226$
Z3	10.15 ± 2.54	$D_{(100)} = 10.09$ $D_{(002)} = 11.84$ $D_{(101)} = 7.59$	$a = 3.267$ $c = 5.234$
Z4	6.60 ± 1.62	$D_{(100)} = 6.10$ $D_{(002)} = 5.64$ $D_{(101)} = 6.49$	$a = 3.247$ $c = 5.203$

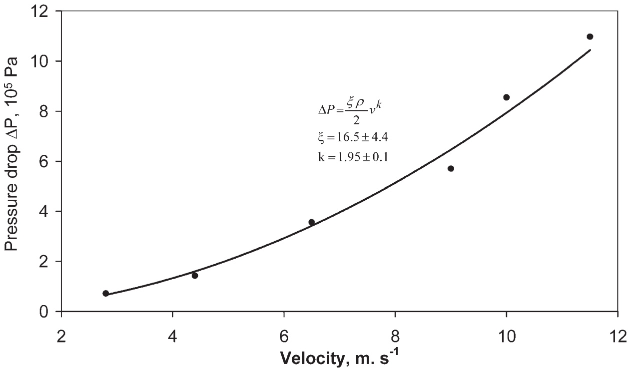

Figure 5. Pressure drop through the T-mixer vs. fluid velocity for diethylene glycol at 353 K.

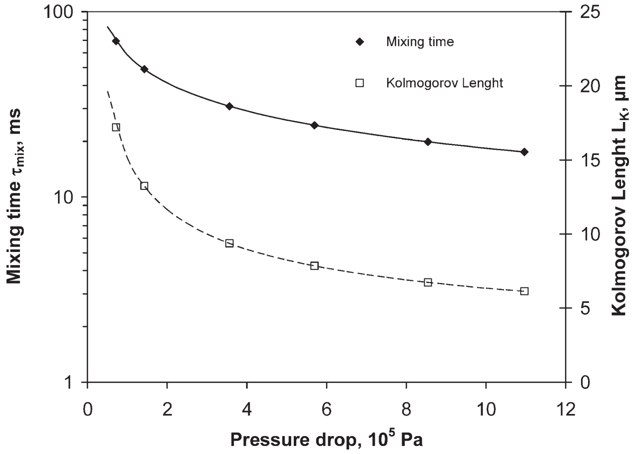

Figure 6. Mixing time and Kolmogorov length vs. pressure drop through the T-mixer for diethylene glycol at 353 K.

geometry and such properties of the fluid as density and viscosity using the relationship

$$P=N_p\rho N^3D^5 \tag{4}$$

For a straight paddle impeller in the turbulent regime,[63] N_p is approximately equal to 2, and hence, one can estimate ε from the data of Table 1. For the stirred reactor experiments, because mass density is not sensitive to the temperature, the dissipation energy ε is approximately 0.83 W kg^{-1} and is almost the same for the Z0 and Z1 experiments, whereas the Kolmogorov lengths are respectively equal to 100.5 and 39.9 µm for the Z0 and Z1 experiments.

In the case of the T-mixer, the power dissipated to feed the T-mixer is given by the product of the pressure drop and the flow rate, $\Delta P \times Q$.[42] The ratio of this power to the solution mass contained in the T-mixer defines the mean specific power dissipated in the mixer per unit mass of the solution as given in Eq. 5

$$\varepsilon=\frac{\Delta PQ}{\rho V_{\mathrm{mix}}} \tag{5}$$

where ΔP is the pressure drop through the T-mixer, Q is the flow rate, ρ is the liquid mass density, and V_{mix} is the mixer volume.

The flow rate Q was estimated from the flow velocity in the main duct of the T-mixer, which varies nearly linearly with the square root of the pressure applied to the buffer solutions.[42] This situation enables definition of a pressure drop coefficient ξ via relationship (6), as shown in Figure 5

$$\Delta P=\frac{\xi\rho}{2}v^k \tag{6}$$

The mixing time could be estimated in the case of a turbulent flow regime from a theoretical point of view. The principle is based on the fact that a relationship exists between changes in the concentration and velocity fluctuations during mixing. For liquids with a high Schmidt number ($Sc >> 1$), the rate of decay of the concentration variance in isotropic and homogeneous turbulence is a first-order process with a time constant given by Corrsin[64]

$$\tau_{\mathrm{mix}}=2\left(\frac{L^2}{\varepsilon}\right)^{\frac{1}{3}}+\frac{1}{2}\left(\frac{v}{\varepsilon}\right)^{\frac{1}{2}}\ln(Sc) \tag{7}$$

where the Schmidt number is calculated from the kinematic viscosity v and the diffusion coefficient of species D_{AB} by

$$Sc=\frac{v}{D_{\mathrm{AB}}} \tag{8}$$

For a given species, the mixing time τ_{mix} in the first term in Eq. 7 is controlled locally by the time required for the largest scale L of the concentration fluctuation and reduced to the smallest scale of Batchelor through the Kolmogorov scale. The second term in Eq. 7, which refers to fine-scale mixing, was refined to apply to sizes below the Kolmogorov velocity microscale. In the specific case of the T-mixer, as shown in Figure 6, increasing the pressure drop simultaneously decreases the Kolmogorov length scale and the mixing time.

Table 3 summarizes the mixing characteristics of the stirred reactor and the T-mixer. We clearly note the existence of a correlation between the size distributions obtained from TEM and XRD and the calculated length and time scales.

From the results of Table 3, we can notice that increasing the turbulence intensity drastically decreases the mixing time and the Kolmogorov lengths, thereby improving micro- and macromixing. Although micromixing takes place over length scales ranging from the Kolmogorov length to the molecular mean free path length, macromixing ensures feed reagents on the scale of the order of the small turbulence eddy length scale, that is, the Kolmogorov length. The intensification of turbulence leads to smaller eddies, shorter characteristic times of molecular diffusion at the eddy length scale, and therefore, to faster mixing. For a given chemistry time-scale, decreasing the mixing time produces a Damköhler number $Da <<1$. The Damköhler number is calculated in this work as the ratio between the mixing and the precipitation times, which is normally considered as an instantaneous reaction. Nevertheless, the process could be divided into sequential steps including: (i) solvation, (ii) nucleation, (iii) crystal growth, (iv) coagulation, and (v) Ostwald ripening. Each

Table 3. Mixing Characteristics

Experiment	Pressure drop $\Delta P \times 10^5$ Pa	Dissipated energy ε, W kg^{-1}	Kolmogorov length L_K, µm	Mixing time τ_{mix}, s
Z1	–	0.83	39.9	1.119
Z4	5	18 347	8.2	0.026

step has its own characteristic time, which could be compared with the mixing time.

Solvation time, τ_{solv}

For the stirred reactor, the zinc acetate is introduced in solid form and mixed with the DEG, and the first step consists of the solvation of the metallic salt by the polyol. Nevertheless, according to Bilecka et al.,[60] the formation of ZnO nanoparticles necessitates an additional step of monomer formation by an esterification reaction between acetic acid and alcohol. In their system, synthesis of ZnO nanoparticles was performed using benzyl alcohol and assisted by microwave heating. This latter process permitted the improvement of the esterification step, which is assumed to be a first-order reaction with the zinc acetate concentration and leads to a reaction constant of $k_{\mathrm{est}} = 2.36 \times 10^{-4}\ \mathrm{s}^{-1}$ at 395 K ($\tau_{\mathrm{solv}} = 4.2 \times 10^{3}$ s) with thermal heating and $k_{\mathrm{est}} = 2.88 \times 10^{-3}\ \mathrm{s}^{-1}$ ($\tau_{\mathrm{solv}} = 3.47 \times 10^{2}$ s) at 393 K with microwave heating. The evident advantage of microwave heating is a significant reduction in the solvation time. Using DEG as the solvent permits us to obtain an intermediate value of ($\tau_{\mathrm{solv}} = 1.2 \times 10^{3}$ s) in our thermally heated stirred reactor at 403 K, which is estimated from the time required to transform the transparent initial solution to a white turbid solution. Compared with benzyl alcohol, DEG presents two alcohol groups that could enhance the esterification step. For the impinging jet and T-mixer experiments, the solvation and esterification steps were performed outside of the mixer apparatus and will not be considered in this work.

Nucleation time, τ_{nuc}

For the nucleation step (ii), the nucleation time can be estimated from the classical theory, assuming homogeneous nucleation and supersaturation (*S*) as drivingforce. Indeed, the ZnO concentration in the polyol easily exceeds its low solubility, thus increasing the supersaturation-enhanced ZnO nucleation. Because no seed or foreign particles exist in the solvent, we can assume homogeneous nucleation. Although we have used homogeneous nucleation theory,[65,66] the possibility of heterogeneous nucleation still exists. For nanoparticle nucleation, the critical size typically ranges from 2 to 6 molecules, depending on the type of solute and solvent.[20,67–69] For instance, the critical number of 2 and the solid-liquid energy were adapted from Ref. [70 for zinc oxide nanoprecipitation in alcohols

$$
\begin{aligned}
k_n &= 0 \quad \text{for}\, l < l_{\mathrm{c}} \\
k_n &= A \exp\left[-\frac{16\pi\sigma^3 V_m^2}{3(k_{\mathrm{B}}T)^3(\ln s)^2}\right] \text{for}\, l \geq l_{\mathrm{c}}
\end{aligned}
\tag{9}
$$

where l_{c} is taken as equal to 2 molecules of zinc oxide (as suggested by Layek et al.[70]), A is the pre-exponential factor, σ is the solid-liquid interfacial energy of the nucleus with the solvent, V_{m} is the volume of a ZnO molecule, k_{B} is the Boltzmann constant, T is reaction temperature, and $s = C/C_{\mathrm{s}}$ is the degree of supersaturation in the liquid phase. In this work, C_{s} is the solubility of ZnO, and C is the concentration of ZnO molecules in the solvent at any instant of time. Hu et al.[71] reported the solubility of ZnO nanoparticles in a series of *n*-alkanols from ethanol to 1-hexanol. Their results showed that nucleation and growth in ethanol and 1-propanol were retarded compared to longer chain length alcohols, where nucleation and growth were faster. Due to the lack of data for zinc oxide growth in DEG, we fitted the data from the model of Layek et al.[70] in which zinc oxide nanoparticles were grown in a stirred tank using either methanol or ethanol as solvents. From these results, the researchers found that solvents of lower carbon chain-length and lower temperature growth independently reduce the particle size to between 1.5 and 5 nm. This observation is in agreement with our results because we worked with higher carbon chain-length and higher temperatures, and thus, the obtained ZnO sizes were obviously higher. As a first approximation, we estimate the nucleation time from a solution concentration assumed to be C–C_0, where C_0 is the initial molar concentration of dissolved ZnO molecules in the solution. Using the data of Table 4 leads to a nucleation time of ZnO in DEG of $\tau_{\mathrm{nuc}} = 6.1 \times 10^{-31}$ s at 403 K for a stirred reactor. In contrast, for a T-mixer, because the mixing volume is smaller, the nucleation time is reduced to $\tau_{\mathrm{nuc}} = 2.0 \times 10^{-28}$ s. In both situations, the nucleation time is notably short because the ZnO concentration in the solvent easily exceeds its notably low solubility, thus quickly rendering the solution supersaturated. A parametric variation of the supersaturation does not significantly affect the nucleation time because supersaturation appears as the inverse of $(\ln(s))^2$ in the exponential term of Eq. 9. Indeed, a sensitivity study of the Eq. 9 obtained by varying the supersaturation by several orders of magnitude will slightly vary the nucleation rate k_{n} and hence the nucleation time. The results of nucleation time are summarized in Figure 7.

Growth time, τ_g

Growth of individual ZnO nanoparticles was estimated from the individual nanoparticle size *d* as measured by XRD and the diffusion of dissolved ZnO molecules from the solvent onto the particle surface. The diffusion layer thickness was assumed to be equal to the nanoparticle radius.[70] Due to the high surface energy of the nanoparticle, the monomer incorporation into the nanoparticle matrix was reasonably assumed to be rapid relative to the liquid diffusion. According to Eq. 10, the growth can be represented by a ZnO diffusion equation in which the total flux of ZnO molecules to the surface represented by the left term in Eq. 10 is balanced by the growth rate of an individual nanoparticle given by the right term

$$
4\pi r^2 k_{\mathrm{G}}(C - C_i) = \frac{d}{dt}\left(\frac{v}{V_{\mathrm{m}} N_{\mathrm{A}}}\right) \text{with}\, k_{\mathrm{G}} = \frac{D_{\mathrm{AB}}}{r} \tag{10}
$$

where r is the nanoparticle radius estimated from XRD measurements, k_{G} is the mass transfer coefficient, D_{AB} is the diffusion coefficient of ZnO in DEG, C and C_{i} are the ZnO concentrations in the solvent and at the solid-liquid interface, respectively, t is the time, v is the volume of the growing nanoparticle, V_{m} is the molecular volume of ZnO, and N_{A} is Avogadro's number. For an instantaneous surface reaction, the concentration of ZnO at the interface is equal to its solubility, that is, $C_{\mathrm{i}} \approx C_{\mathrm{s}}$. The diffusion controlled growth rate of a particle of radius r is thus written as

$$
\frac{dv}{dt} = 4\pi V_{\mathrm{m}} N_{\mathrm{A}} D_{\mathrm{AB}} C \left(\frac{3v}{4\pi}\right)^{\frac{1}{3}}
$$

By substituting the volume of the particle assumed to be spherical shape, $v = 4/3\ \pi r^3$ and integrating the radius between the initial radius r_0 (r_0 is negligible as compared to

Table 4. List of Parameters Used in Time Scale Analysis

Parameter	Value	Source
Initial ZnO concentration C_0	200 mM	This work
Mixing volume V	Stirred tank: 2×10^{-4} m^3 T-mixer[a]: 6.3×10^{-7} m^3	This work
Temperature T	353 K and 403 K	This work
Particle diameter after growth, d	Stirred tank at 403 K: 1.44×10^{-8} m T-mixer at 353 K: 5.64×10^{-9} m	This work
Particle diameter after coagulation, d'	Stirred tank at 403 K: 1.916×10^{-8} m T-mixer at 353 K: 6.60×10^{-9} m	This work
Diffusion coefficient of ZnO in DEG D_{AB}	1.62×10^{-10} m^2 s^{-1} (353 K) 6.60×10^{-10} m^2 s^{-1} (403 K)[b]	Ref. 52
Pre-exponenential factor A	1×10^{34} m^{-3} s^{-1}	Ref. 70
Surface energy σ	0.1 J m^{-2}	Ref. 70
ZnO molecular volume V_m	2.41×10^{-29} m^3 per molecule	Ref. 70
ZnO solubility in DEG C_s	3.01×10^{-09} mol m^{-3} (353 K) 1.34×10^{-08} (403 K)	Fitted from Ref. 70
Inverse of the correction factor for dipole−dipole and van der Waal's interactions 1/W	1.51 (353 K) 1.47 (403 K)	Fitted from Ref. 70
Coagulation efficiency β	6.51×10^{-07} (353 K) 8.60×10^{-07} (403 K)	Fitted from Ref. 70
$\tau_{coa} = 1/K_{coa}$	Z1:1.26×10^2 s Z4: 4.83×10^2 s	This work
k_{OR}	4.97×10^{-29} m^3 s^{-1} (353 K) 3.22×10^{-29} m^3 s^{-1} (403K)	Fitted from Ref. 70
τ_{OR}	Z1: 1.22×10^5 s Z4: 1.8×10^3 s	This work

[a] Approximated by the exit tube volume as an upper bound.
[b] From Wilke and Chang Correlation.[52]

r since we considered a cluster of 2 atoms) and the final particle radius r, the growth time expression is hence simplified to

$$\tau_g = \frac{1}{2\pi d N_A D_{AB} C} \tag{11}$$

Calculating τ_g in our conditions with the data listed in Table 4 leads to a growth time of $\tau_g = 1.37 \times 10^{-10}$ s for the stirred reactor at 403 K and $\tau_g = 1.34 \times 10^{-09}$ s for the T-mixer at 353 K. The diffusive growth scales are summarized in Figure 7.

For conditions of forced convection in steady flows, the solid-liquid mass transfer coefficient can be estimated from the Frossling equation.[72] For particles whose largest size dimension is smaller than Kolmogorov's length scale, Armenante and Kirwan[73] proposed and validated the finding that the turbulent contribution to mass transfer is via the boundary layer development resulting from the exchange of particles among decaying eddies, which can be characterized by

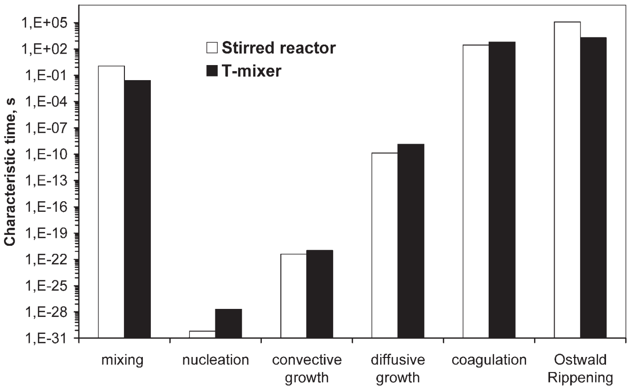

Figure 7. Calculated characteristic times of nucleation, growth, mixing, coagulation, and Ostwald ripening for stirred reactor and T-mixer.

$$Sh = 2 + 0.52 Re^{0.52} Sc^{1/3} \quad \text{for}\, d \leq L_K \tag{12}$$

where $Sh = k_G\, d/D_{AB}$ is the Sherwood number, and Re and Sc are the Reynolds and Schmidt numbers, respectively. As plotted in Figure 7, accounting for convective mass transfer reduces the characteristic time of growth to approximately10^{-21} s.

Coagulation time, τ_{coa}

High supersaturation levels, and therefore, the rapid formation of huge numbers of nuclei increase the tendency of the particles to aggregate with weak cohesive forces and to agglomerate with strong interparticleforces.[74] The kinetics of Brownian coagulation of monodisperses particles at the early stage can be described by a n-order process $dN/dt = -k\, N^n$ where N is the total number concentration of particle, k is the coagulation rate constant, and n is the order.[75] Thompson et al.[76] proposed that in a dispersed system of particles with small diameter and low concentration, the agglomeration of particles can be treated like a simple chemical reaction with $n = 1$; As suggested by Smoluchowski,[77] Brownian motion leads to perikinetic aggregation represented by a linear variation of the cube of the particle diameter $d^3\,(t) = A1\ + B1\ t$, with $A1$ and $B1$ a model constants. This process can be enhanced through shear stress in the so called orthokinetic. Aggregation for agitated systems is then represented by log

$d(t) = A2 + B2t$, with $A2$ and $B2$ a time-independent constants. Di Pasquale et al.[32] correlated the relative significance among the Brownian and turbulent kernel through the Péclet number (Pe). In their model, due to frequent collisions, aggregation, is a second order process. In this work, coagulation by the self-organization of two nanoparticles of diameter d to form a larger crystal of diameter d' that share a common crystallographic orientation was considered via the well-known oriented attachment (OA) mechanism first proposed by Penn[78] and recently reviewed by Zhang et al.[79] and Lv et al.[80] In the case of wurtzite zinc oxide, the crystal grows along the c-axis and is composed of eight faces. The bottom and top faces are terminated by polar Zn^{2+} and O^{2-}, and the six remaining planes are nonpolar.[69] Hence, ZnO coagulation of particles with the same crystallographic orientation occurs in two steps, including attachment of two particles by Brownian collision and subsequent fusion into a larger particle via solid-state diffusion. In this process, the planes with the highest surface energy disappear to reduce the overall energy of the system. To estimate the coagulation time, Layek et al.[70] modified the frequency of Brownian collision to incorporate the effect of dipole–dipole van der Waal's interactions and the probability of OA

$$q_{\text{coa}} = \frac{1}{32}\left(\frac{1}{w}\right)\frac{2k_B T}{3\mu}\left[2+\left(\frac{v_1}{v_2}\right)^{1/3}+\left(\frac{v_2}{v_1}\right)^{1/3}\right] \tag{13}$$

where 1/32 is the attachment probability because only 2 out of 64 relative positions of the individual nanoparticle can result in a favorable orientation for fusion[70] and W is the correction factor for dipole–dipole and van der Waal's interactions that is temperature dependent. The volumes v_1 and v_2 are relative to the two colliding nanoparticles, and μ is the viscosity of the solvent. For particles of the same volume, the collision frequency q_{coa} is hence simplified to

$$q_{\text{coa}} = \frac{1}{32}\left(\frac{1}{w}\right)\frac{8k_B T}{3\mu} \tag{14}$$

The coagulation rate k_{coa} is obtained by taking into account the efficiency of the collision between two nanoparticles

$$k_{\text{coa}} = \beta q_p N_0 \tag{15}$$

where β is the coagulation efficiency defined as the fraction of collisions that lead to successful coagulation, and N_0 is the total number density of ZnO nanoparticles after the nucleation and diffusion growth steps. Since agglomeration is a mass-conserving, but number-reducing process that shifts the particle distribution toward larger sizes, N_0 was calculated by stoichiometric considerations as

$$N_0 = \frac{6C_0 V_m N_A}{\pi d^3} \tag{16}$$

where d is the mean particle diameter taken from XRD measurements in our case, and C_0 is the molar concentration of dissolved ZnO molecules in the solution at time $t = 0$. Accounting for the specific conditions of the experiments Z1–Z4, we obtain the time of coagulation plotted in Figure 7.

Finally, growth timescale τ_g is calculated based on the growth of a single nucleus ($l_c = 2$) by diffusional-addition of one ZnO molecule and coagulation timescale τ_{coa}, is calculated based on the collision-induced addition of another ZnO nucleus by OA. The efficiency of the collision between two nanoparticules β was fitted from Ref. [70 and given in Table 4. Assuming that the kinetics coagulation is a first order process[78]

$$\tau_{\text{coa}} = \frac{1}{k_{\text{OA}}} \tag{17}$$

Ostwald ripening time, τ_{OR}

Finally, the coarsening effects that are controlled either by mass transport or diffusion are often referred to as the Ostwald ripening process. This diffusion-limited process is the most predominant growth mechanism.[81–83] Indeed, for the growth of the ZnO nanoparticles from the dissolution of the coexisting smaller particles, this process is diffusion controlled, and the rate of this diffusion-controlled process is expressed by

$$\tau_{\text{OR}} = \frac{d'^3 - d^3}{k_{\text{OR}}} \tag{18}$$

where d'^3 and d^3 are the cube of the average final and initial particle diameters, respectively. Due to the high temperature and high turbidity, it was not possible to dynamically monitor the nanoparticle diameters during growth. Hence, d' and d were considered from TEM and XRD measurements, respectively, and the rate constant k_{OR} was extrapolated from the data of Ref. [70 and reported in Table 4.

Conclusions for time scales

Figure 7 summarizes the characteristic times for elementary growth and mixing steps that occur in the extreme mixing configurations namely the stirred reactor and the T-mixer. The notably low values of nucleation time imply that the process is not limited by nucleation, which is quasiexplosive. After massive nuclei formation, the growth step occurs via diffusive or convective mass transfer, which is also rather fast. For the stirred reactor, the highest temperature leads to a shorter growth time and larger particle sizes. During the nucleation and growth steps, mixing ensures the spatially homogeneous concentration of the monomer. However, because the mixing time $\tau_{\text{mix}} < \tau_{\text{coa}} < \tau_{\text{OR}}$, we can conclude that mixing significantly affects the coagulation by OA and the Ostwald ripening steps, thus explaining the disparity of diameters observed in Figure 3. As a consequence, the mixing quality of the reagents is a key parameter for controlling both the size and polydispersity of the ZnO nanoparticles produced by the polyol method. Smaller sizes and narrower distributions of nanoparticles require a high mixing intensity and are obtained for the T-mixer.

Spatial scale of the process

The measured ZnO particle sizes vs. dissipated energy (ε) is presented in Figure 8. Increasing the dissipated energy by almost four orders of magnitude decreases the size of the nanoparticles.

When plotted vs. the Kolmogorov length (L_K) of the mixing scale in Figure 9, the particle size is correlated with the Kolmogorov length (L_K). This choice of presentation is explained by the fact that the spatial homogeneity scale of the reactions is divided by the fluid eddies obtained after the injected energy dissipation. The eddies can be characterized according to their geometry as objects whose dimension can vary from layered (1-D) to cylindrical (2-D) and bubbled (3-D). As a result, the rapid nanoparticle nucleation begins at

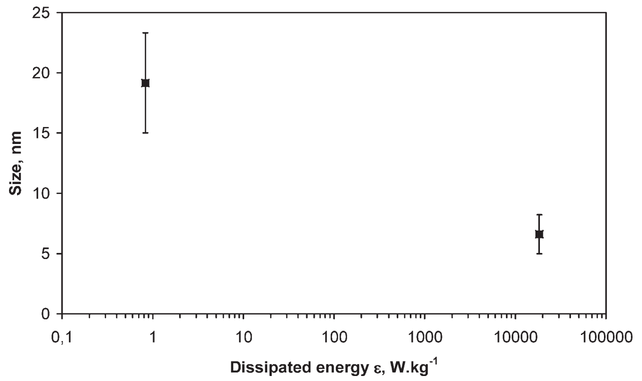

Figure 8. Size of ZnO nanoparticles vs. dissipated energy summarized for stirred reactor and T-mixer.

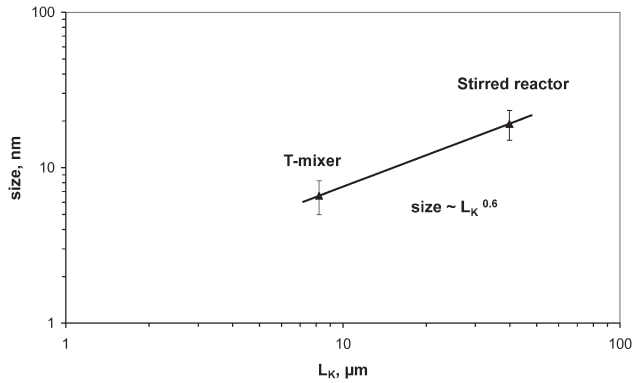

Figure 9. Size of ZnO nanoparticles vs. Kolmogorov length summarized for stirred reactor and T-mixer.

the eddy boundaries, and the involved nanoparticle mass (M_{NP}) can be proportional to the smallest characteristic eddy volume $L_K^{\,D}$, where D is equal to 1, 2, and 3, respectively, for 1-D, 2-D, and 3-D geometries. Because the obtained nanoparticles are compact nonfractal objects ($M \propto \text{size}^3$), their sizes can be related to this mass as size $\propto L_K^{D/3}$. The linear fit of data in Figure 9 in the logarithmic frame results in a turbulent eddy geometry with $D/3 = 0.6 \pm 0.2$, which

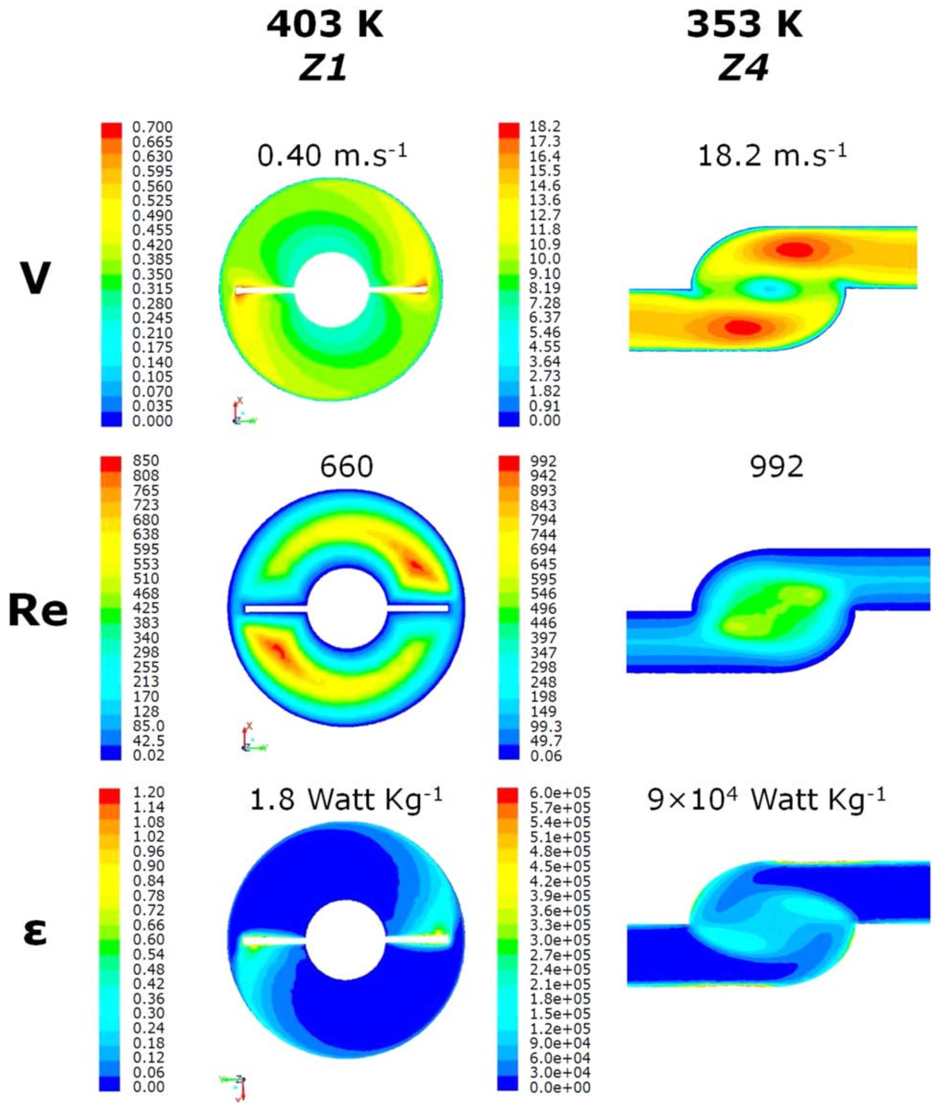

Figure 10. Calculated contours of velocity *v* (m s^{-1}), Reynolds number *Re* and energy dissipation ε (W kg^{-1}) in transversal planes of stirred reactor at 403 K (Z1) and T-mixer at 353 K (Z4).

[Color figure can be viewed in the online issue, which is available at wileyonlinelibrary.com.]

permits their description as an approximation of the 2-D geometry or $D = 1.8$. At the same time, a significant dispersion of the eddy geometry can be suggested by expanding from the quasi-1-D to the quasi-3-D case.

The above relationship between the nanoparticle geometry and micromixing scale reflects an interaction between the timescales of chemical reactions and the dissipation of eddies down to the molecular level and may be characteristic of the polyol process. Additional experimental data are required to validate this hypothesis.

CFD modeling

To spatially quantify micromixing intensity, we carried out numerical simulations of the flow behavior in the extreme cases of stirred tank and T-mixer configurations. In the case of impinging free-jets, the formation and break up of the liquid sheet at the exit of the cylindrical jets involves much more complex physical phenomena as atomization, instability of sheets and rims, wave motions necessitating more sophisticated numerical models. The simulation of the mixing in TIJ was not considered in this work since it necessitate an improved volume-of-fluid method augmented with adaptive mesh refinement as discussed by Chen et al.[47] To simulate stirred tank and T-mixer configurations, we used the commercial numerical tool Fluent from ANSYS.[84] This tool uses a finite volume method to calculate the flow and the diffusion in three spatial dimensions. The 3-D geometry was created using ANSYS Design Modeller and the mesh was generated using ANSYS Meshing application. The impeller rotation was modelled using the multiple reference frame approach, where the computational grid comprised two meshes: an inner rotating volume enclosing the impeller and an outer stationary volume forming the rest of the reactor and separated by an interface. The interface was defined by the program as an imaginary section to provide the interaction between the rotating and stationary frame. In the case of the T-mixer, we used a pressure-based solution approach suitable for incompressible flows. The flow equations were solved in the 3-D domain defined by the T-mixer geometry, and an unstructured nonuniform tetrahedral mesh was generated inside the computational domains. After numerous checks for grid sensitivity and mesh constraints, the total number of elements was approximately 335,000 for the batch reactor and approximately 4,000,000 for the T-mixer, leading to a final grid with 90,000 and 718,000 nodes, respectively, and an average grid skewness of 0.2. As expected, the fluid flow quantified by velocity, *Re*, and energy dissipation (Figure 10) is more intense and better spatially distributed in the T-mixer at 353 K than in the stirred reactor at 403 K.

We can conclude that with an increase of the turbulence intensity, the mixing processes intensify on the micro- and macroscales. Although micromixing takes place over length scales ranging from the Kolmogorov length to the molecular mean free path length, macromixing ensures the presence of feed components at a scale on the order of the small turbulence eddy length scale, that is, the Kolmogorov length. Consequently, the characteristic size of the small turbulence eddies defines the characteristic time for micromixing, which also corresponds to the characteristic time of the diffusion through an elementary eddy. The intensification of turbulence leads to smaller eddies, shorter characteristic times for molecular diffusion at the eddy length scale, and therefore, to faster physical mixing (mixture homogenizing). If the *Re* is sufficiently high, the characteristic mixing time can drop below the chemistry time-scale. In this case, the particle precipitation process is determined only by the nucleation and growth kinetics. Such a situation corresponds to small Damköhler numbers, $Da \leq 1$. Reaching this, high *Re* limit will lead to advanced fluid homogenization and a targeted smaller size and narrower size distribution of nanoparticles.[21]

Conclusions

In this work, we investigated three mixing configurations used to produce zinc oxide nanoparticles in a polyol medium. In the stirred laboratory-scale configuration, the synthesis at 353 K did not lead to production of nanoparticles. Increasing the temperature in the stirred reactor or improving the energy dissipation by use of a T-mixer or impinging jets produced well-crystallized zinc oxide as characterized by TEM and XRD. In addition, the mean size and polydispersity of the generated nanoparticles are closely related to the energy dissipation and hence to the micromixing quality. The impinging jet configuration with manual injection of the reagents via syringes offers an intermediate economical solution to produce nanoparticles via precipitation in a confined space. A flash nanoprecipitation process via reactive impingement mixing is already in use in several biological laboratories to produce small quantities of drugs in the form of core-shell or functionalized nanoparticles. The simplest way to achieve such rapid mixing is to use double or multiple injections to feed the reagents, which is more convenient and faster to install than CIJ and MIV reactors. Reagent injection could be improved by adding an automatic syringe pump to increase the pressure drop and hence the energy dissipation. Finally, we compared mixing times with different chemical times, including nucleation, diffusive, and convective growth, coagulation by OA, and Ostwald ripening in the specific case of polyol precipitation. Indeed, this medium is characterized by a high viscosity and low diffusion coefficients that affect the mass transport and reaction kinetics. The richness of the polyol process associated with the efficiency of the T-mixer will certainly provide opportunities for the synthesis of several classes of nanomaterials with controlled size and uniformity.

Acknowledgments

IFR Paris Nord Plaine de France (PPF), « ANR (Agence Nationale de la Recherche) and CGI (Commissariat à l'Investissement d'Avenir) are gratefully acknowledged for their financial support of this work through Labex SEAM (Science and Engineering for Advanced Materials and devices) ANR 11 LABX 086, ANR 11 IDEX 05 02 ».

Literature Cited

1. Kolmogorov AN. The local structure of turbulence in incompressible viscous fluid for very large Reynolds numbers. *Proc Math Phys Sci.* 1991;434(1890):9–13.
2. Bakker RA. *Micromixing in Chemical Reactors: Models, Experiments and Simulations.* PhD: Nederland, Delft University of Technology, 1996.
3. Baldyga J, Bourne JR. *Turbulent Mixing and Chemical Reactions.* Chichester: Wiley, 1999.
4. Pope SB. *Turbulent Flows.* Cambridge: Cambridge University Press, 2000.
5. Gradl J, Schwarzer H-C, Schwertfirm F, Manhart M, Peukert W. Precipitation of nanoparticles in a T-mixer: coupling the particle population dynamics with hydrodynamics through direct numerical

simulation. *Chem Eng Process: Process Intensification*. 2006;45(10): 908–916.

6. Marchisio DL, Barresi AA, Garbero M. Nucleation, growth, and agglomeration in barium sulfate turbulent precipitation. *AIChE J*. 2002;48(9):2039–2050.
7. Schwarzer H-C, Schwertfirm F, Manhart M, Schmid H-J, Peukert W. Predictive simulation of nanoparticle precipitation based on the population balance equation. *Chem Eng Sci*. 2006;61(1):167–181.
8. Bałdyga J, Makowski Ł, Orciuch W. Double-feed semibatch precipitation effects of mixing. *Chem Eng Res Des*. 2007;85(5):745–752.
9. Lince F, Marchisio DL, Barresi AA. Strategies to control the particle size distribution of poly-ε-caprolactone nanoparticles for pharmaceutical applications. *J Colloid Interface Sci*. 2008;322(2):505–515.
10. Harnby N, Edwards MF, Nienow AW. *Mixing in the Process Industries*. Oxford: Butterworth-Heinemann, 1997.
11. Villermaux J. *A Simple Model for Partial Segregation in a Semi-Batch Reactor*. AIChE Annual Meeting, San Francisco, 1989: Paper 114a.
12. Villermaux J, Falk L. A generalized mixing model for initial contacting of reactive fluids. *Chem Eng Sci*. 1994;49(24, Part 2):5127–5140.
13. Marmo L, Manna L, Chiampo F, Sicardi S, Bersano G. Influence of mixing on the particle size distribution of an organic precipitate. *J Cryst Growth*. 1996;166(1–4):1027–1034.
14. Mahajan AJ, Kirwan DJ. Micromixing effects in a two-impinging-jets precipitator. *AIChE J*. 1996;42(7):1801–1814.
15. Bockhorn H, Mewes D, Peukert W, Warnecke H-J. *Micro and Macro Mixing Analysis, Simulation and Numerical Calculation*. Berlin: Springer-Verlag, 2010.
16. Randolph AD, Larson MA. *Theory of Particulate Processes, Analysis and Techniques of Continuous Crystallization*. Université du Michigan: Academic Press, New York, 1971.
17. van Embden J, Sader JE, Davidson M, Mulvaney P. Evolution of colloidal nanocrystals: theory and modeling of their nucleation and growth. *The Journal of Physical Chemistry C*. 2009;113(37):16342–16355.
18. Sajjadi S. Population balance modeling of particle size distribution in monomer-starved semibatch emulsion polymerization. *AIChE J*. 2009;55(12):3191–3205.
19. Alamir M, Sheibat-Othman N, Othman S. Measurement based modeling and control of bimodal particle size distribution in batch emulsion polymerization. *AIChE J*. 2010;56(8):2122–2136.
20. Ethayaraja M, Bandyopadhyaya R. Population balance models and Monte Carlo simulation for nanoparticle formation in water-in-oil microemulsions: implications for CdS synthesis. *J Am Chem Soc*. 2006;128(51):17102–17113.
21. Li J, Rodrigues M, Paiva A, Matos HA, Gomes de Azevedo E. Modeling of the PGSS process by crystallization and atomization. *AIChE J*. 2005;51(8):2343–2357.
22. Bałdyga J, Orciuch W. Barium sulphate precipitation in a pipe—an experimental study and CFD modelling. *Chem Eng Sci*. 2001;56(7): 2435–2444.
23. Falk L, Schaer E. A PDF modelling of precipitation reactors. *Chem Eng Sci*. 2001;56(7):2445–2457.
24. Jaworski Z, Nienow AW. CFD modelling of continuous precipitation of barium sulphate in a stirred tank. *Chem Eng J*. 2003;91(2–3):167–174.
25. Rousseaux JM, Vial C, Muhr H, Plasari E. CFD simulation of precipitation in the sliding-surface mixing device. *Chem Eng Sci*. 2001; 56(4):1677–1685.
26. Wang L, Fox RO. Application of in situ adaptive tabulation to CFD simulation of nano-particle formation by reactive precipitation. *Chem Eng Sci*. 2003;58(19):4387–4401.
27. Wei H, Zhou W, Garside J. Computational fluid dynamics modeling of the precipitation process in a semibatch crystallizer. *Ind Eng Chem Res*. 2001;40(23):5255–5261.
28. Bakldyga J, Podgórska W, Pohorecki R. Mixing-precipitation model with application to double feed semibatch precipitation. *Chem Eng Sci*. 1995;50(8):1281–1300.
29. Barresi AA, Marchisio D, Baldi G. On the role of micro- and meso-mixing in a continuous Couette-type precipitator. *Chem Eng Sci*. 1999;54(13–14):2339–2349.
30. Johnson BK, Prud'homme RK. Flash nanoprecipitation of organic actives and block copolymers using a confined impinging jets mixer. *Aust J Chem*. 2003;56(10):1021–1024.
31. Johnson BK, Prud'homme RK. Chemical processing and micromixing in confined impinging jets. *AIChE J*. 2003;49(9):2264–2282.
32. Di Pasquale N, Marchisio DL, Barresi AA. Model validation for precipitation in solvent-displacement processes. *Chem Eng Sci*. 2012; 84(0):671–683.
33. Cheng JC, Fox RO. Kinetic modeling of nanoprecipitation using CFD coupled with a population balance. *Ind Eng Chem Res*. 2010; 49(21):10651–10662.
34. Mühlenweg H, Gutsch A, Schild A, Pratsinis SE. Process simulation of gas-to-particle-synthesis via population balances: investigation of three models. *Chem Eng Sci*. 2002;57(12):2305–2322.
35. Zauner R, Jones AG. On the influence of mixing on crystal precipitation processes—application of the segregated feed model. *Chem Eng Sci*. 2002;57(5):821–831.
36. Liu H, Li J, Sun D, Odoom-Wubah T, Huang J, Li Q. Modeling of silver nanoparticle formation in a microreactor: reaction kinetics coupled with population balance model and fluid dynamics. *Ind Eng Chem Res*. 2014;53(11):4263−4270.
37. Favero JL, Silva LFLR, Lage PLC. Comparison of methods for multivariate moment inversion—introducing the independent component analysis. *Comput Chem Eng*. 2014;60(0):41–56.
38. Fiévet F, Brayner R. The Polyol Process. In: Brayner R, Fiévet F, Coradin T, editors. *Nanomaterials: A Danger or a Promise?* London: Springer, 2013:1–25.
39. Figlarz M, Fiévet F, Lagier JP. French patent, No. 8221483, 1985.
40. Poul L, Ammar S, Jouini N, Fievet F, Villain F. Synthesis of inorganic compounds (metal, oxide and hydroxide) in polyol medium: a versatile route related to the sol-gel process. *J Sol-Gel Sci Technol*. 2003;26(1–3):261–265.
41. Dakhlaoui A, Jendoubi M, Smiri LS, Kanaev A, Jouini N. Synthesis, characterization and optical properties of ZnO nanoparticles with controlled size and morphology. *J Cryst Growth*. 2009;311(16):3989–3996.
42. Azouani R, Michau A, Hassouni K, et al. Elaboration of pure and doped TiO2 nanoparticles in sol–gel reactor with turbulent micromixing: application to nanocoatings and photocatalysis. *Chem Eng Res Des*. 2010;88(9):1123–1130.
43. Santillo G, Deorsola FA, Bensaid S, Russo N, Fino D. MoS_2 nanoparticle precipitation in turbulent micromixers. *Chem Eng J*. 2012; 207–208(0):322–328.
44. Winkelmann M, Schuler T, Uzunogullari P, et al. Influence of mixing on the precipitation of zinc oxide nanoparticles with the miniemulsion technique. *Chem Eng Sci*. 2012;81(0):209–219.
45. Bensaid S, Deorsola FA, Marchisio DL, Russo N, Fino D. Flow field simulation and mixing efficiency assessment of the multi-inlet vortex mixer for molybdenum sulfide nanoparticle precipitation. *Chem Eng J*. 2014;238(0):66–77.
46. Bush JWM, Hasha AE. On the collision of laminar jets: fluid chains and fishbones. *J Fluid Mech*. 2004;511:285–310.
47. Chen X, Ma M, Yang V. Dynamics and stability of impinging jets. In: ILASS-Americas, ed. 24th Annual Conference on Liquid Atomization and Spray Systems. San Antonio, TX, May 2012.
48. Hosni M, Kusumawati Y, Farhat S, Jouini N, Pauporté T. Effects of oxide nanoparticle size and shape on electronic structure, charge transport, and recombination in dye-sensitized solar cell photoelectrodes. *J Phys Chem C*. 2014;118(30):16791–16798.
49. Nauman EB. *Chemical Reactor Design, Optimization, and Scaleup*, 2nd ed. Hoboken, New Jersey: Wiley, 2008.
50. Schwarzer H-C, Peukert W. Combined experimental/numerical study on the precipitation of nanoparticles. *AIChE J*. 2004;50(12):3234–3247.
51. Marchisio DL, Rivautella L, Barresi AA. Design and scale-up of chemical reactors for nanoparticle precipitation. *AIChE J*. 2006;52(5):1877–1887.
52. Poling BE, Prausnitz JM, O'Connell JP. *The Properties of Gases and Liquids*, 5th ed. New York: McGraw-Hill, 2001.
53. Haiss W, Thanh NTK, Aveyard J, Fernig DG. Determination of Size and Concentration of Gold Nanoparticles from UV−Vis Spectra. *Anal Chem*. 2007;79(11):4215–4221.
54. Caetano BL, Santilli CV, Meneau F, Briois Vr, Pulcinelli SH. In situ and simultaneous UV−vis/SAXS and UV−vis/XAFS time-resolved monitoring of ZnO quantum dots formation and growth. *J Phys Chem C*. 2011;115(11):4404–4412.
55. Scherrer P. Bestimmung der Grösse und der inneren Struktur von Kolloidteilchen mittels Röntgenstrahlen. Nachrichten von der Gesellschaft der Wissenschaften zu Göttingen, *Mathematisch-Physikalische Klasse* 1918;26:98–100.
56. Langford JI, Wilson AJC. Scherrer after sixty years: a survey and some new results in the determination of crystallite size. *J Appl Crystallogr*. 1978;11(2):102–113.
57. Morkoç H, Özgür Ü. *Zinc Oxide: Fundamentals, Materials and Device Technology*. Germany: Wiley-VCH Verlag GmbH & Co. KGaA, 2009.
58. Seelig EW, Tang B, Yamilov A, Cao H, Chang RPH. Self-assembled 3D photonic crystals from ZnO colloidal spheres. *Mater Chem Phys*. 2003;80(1):257–263.

59. Cheng H-M, Hsu H-C, Chen S-L, et al. Efficient UV photoluminescence from monodispersed secondary ZnO colloidal spheres synthesized by sol–gel method. *J Cryst Growth*. 2005;277(1–4):192–199.
60. Bilecka I, Elser P, Niederberger M. Kinetic and thermodynamic aspects in the microwave-assisted synthesis of ZnO nanoparticles in benzyl alcohol. *ACS Nano*. 2009;3(2):467–477.
61. .ProSimPlus. 2013. *Prosim Plus: Steady-state Simulation and Optimization of Processes*. Available at: www.prosim.net. Accessed May 8, 2014.
62. Fox RO. *Computational Models for Turbulent Reacting Flows*. Cambridge: Cambridge University Press, 2003.
63. Paul EL, Atiemo-Obeng V, Kresta SM. *Handbook of Industrial Mixing: Science and Practice*. Hoboken, New Jersey: Wiley, 2004.
64. Corrsin S. The isotropic turbulent mixer: Part II. Arbitrary Schmidt number. *AIChE J*. 1964;10(6):870–877.
65. Mersmann A. Supersaturation and Nucleation. In: Proceedings of the 13th Symposium on Industrial Crystallization, Toulouse, 16–19 Sept, 1996. *Trans IChemE*. 1996;74(Part A):812–820.
66. Mersmann A. Crystallization and precipitation. *Chem Eng Process: Process Intensification*. 1999;38(4–6):345–353.
67. Ethayaraja M, Dutta K, Bandyopadhyaya R. Mechanism of nanoparticle formation in self-assembled colloidal templates: population balance model and monte carlo simulation. *J Phys Chem B*. 2006; 110(33):16471–16481.
68. Bandyopadhyaya R, Kumar R, Gandhi KS. Modelling of $CaCO_3$ nanoparticle formation during overbasing of lubricating oil additives. *Langmuir*. 2001;17(4):1015–1029.
69. Ethayaraja M, Bandyopadhyaya R. Mechanism and modeling of nanorod formation from nanodots. *Langmuir*. 2007;23(11):6418–6423.
70. Layek A, Mishra G, Sharma A, et al. A generalized three-stage mechanism of ZnO nanoparticle formation in homogeneous liquid medium. *J Phys Chem C*. 2012;116(46):24757–24769.
71. Hu Z, Oskam G, Searson PC. Influence of solvent on the growth of ZnO nanoparticles. *J Colloid Interface Sci*. 2003;263(2):454–460.
72. Mullin JW. *Crystallization*, 4th ed. Oxford U.K.: Elsevier Butterworth-Heinemann; 2001.
73. Armenante PM, Kirwan DJ. Mass transfer to microparticles in agitated systems. *Chem Eng Sci*. 1989;44(12):2781–2796.
74. Wachi S, Jones AG. Dynamic modelling of particle size distribution and degree of agglomeration during precipitation. *Chem Eng Sci*. 1992;47(12):3145–3148.
75. Loria H, Pereira-Almao P, Scott CE. Determination of agglomeration kinetics in nanoparticle dispersions. *Ind Eng Chem Res*. 2011;50(14): 8529–8535.
76. Thompson J, Vasquez A, Hill J, Pereira-Almao P. The synthesis and evaluation of up-scalable molybdenum based ultra dispersed catalysts: effect of temperature on particle size. *Catal Lett*. 2008;123(1–2):16–23.
77. Smoluchowski MV. Drei Vortrage uber Diffusion, Brownsche Molekularbewegung und Koagulation von Kolloidteilchen. *Physik Zeitung*. 1916;XVII:557–599.
78. Penn RL. Kinetics of oriented aggregation. *J Phys Chem B*. 2004; 108(34):12707–12712.
79. Zhang J, Huang F, Lin Z. Progress of nanocrystalline growth kinetics based on oriented attachment. *Nanoscale*. 2010;2(1):18–34.
80. Lv W, He W, Wang X, et al. Understanding the oriented-attachment growth of nanocrystals from an energy point of view: a review. *Nanoscale*. 2014;6(5):2531–2547.
81. Lifshitz IM, Slyozov VV. The kinetics of precipitation from supersaturated solid solutions. *J Phys Chem Solids*. 1961;19(1–2):35–50.
82. Wagner C. Theorie der Alterung von Niederschlägen durch Umlösen (Ostwald-Reifung). *Zeitschrift für Elektrochemie, Berichte der Bunsengesellschaft für physikalische Chemie*. 1961;65(7–8): 581–591.
83. Vollmer J, Papke A, Rohloff M. Ripening and focusing of aggregate size distributions with overall volume growth. *Front Phys*. 2014:2(1–14).
84. ANSYS FLUENT Commercial Software Release 13.0, ANSYS Inc., Canonsburg.

Manuscript received Apr. 22, 2014, and revision received Nov. 27, 2014.